Journal of Pharmaceutical Analysis 15 (2025) 101082

Contents lists available at ScienceDirect

Journal of Pharmaceutical Analysis

journal homepage: www.elsevier.com/locate/jpa

Original article

Peptide-based immuno-PET/CT monitoring of dynamic PD-L1 expression during glioblastoma radiotherapy

Yong Wang [a], Kewen He [a], Yang Zhang [a], Yunhao Chen [a], Shijie Wang [b], Kunlong Zhao [b], Zhiguo Liu [c, **], Man Hu [a, *]

[a] *Department of Radiation Oncology, Shandong Cancer Hospital and Institute, Shandong First Medical University and Shandong Academy of Medical Sciences, Jinan, 250117, China*

[b] *Shandong Provincial Key Laboratory of Radiation Oncology, Shandong Cancer Hospital and Institute, Shandong First Medical University, Shandong Academy of Medical Sciences, Jinan, 250117, China*

[c] *Department of PET/CT Center, Shandong Cancer Hospital and Institute, Shandong First Medical University, Shandong Academy of Medical Sciences, Jinan, 250117, China*

ARTICLE INFO

Article history:
Received 8 April 2024
Received in revised form
17 August 2024
Accepted 21 August 2024
Available online 26 August 2024

Keywords:
PET/CT
Cyclic peptide
PD-L1
Glioblastoma
Radiotherapy

ABSTRACT

Real-time, noninvasive programmed death-ligand 1 (PD-L1) testing using molecular imaging has enhanced our understanding of the immune environments of neoplasms and has served as a guide for immunotherapy. However, the utilization of radiotracers in the imaging of human brain tumors using positron emission tomography/computed tomography (PET/CT) remains limited. This investigation involved the synthesis of [^{18}F]AlF-NOTA-PCP2, which is a novel peptide-based radiolabeled tracer that targets PD-L1, and evaluated its imaging capabilities in orthotopic glioblastoma (GBM) models. Using this tracer, we could noninvasively monitor radiation-induced PD-L1 changes in GBM. [^{18}F]AlF-NOTA-PCP2 exhibited high radiochemical purity (>95%) and stability up to 4 h after synthesis. It demonstrated specific, high-affinity binding to PD-L1 *in vitro* and *in vivo*, with a dissociation constant of 0.24 nM. PET/CT imaging, integrated with contrast-enhanced magnetic resonance imaging, revealed significant accumulation of [^{18}F]AlF-NOTA-PCP2 in orthotopic tumors, correlating with blood-brain barrier disruption. After radiotherapy (15 Gy), [^{18}F]AlF-NOTA-PCP2 uptake in tumors increased from 9.51% ± 0.73% to 12.04% ± 1.43%, indicating enhanced PD-L1 expression consistent with immunohistochemistry findings. Fractionated radiation (5 Gy × 3) further amplified PD-L1 upregulation (13.9% ± 1.54% ID/cc) compared with a single dose (11.48% ± 1.05% ID/cc). Taken together, [^{18}F]AlF-NOTA-PCP2 may be a valuable tool for noninvasively monitoring PD-L1 expression in brain tumors after radiotherapy.

1. Introduction

Glioblastoma (GBM), a highly aggressive and malignant form of brain tumor, represents approximately 16% of all primary brain tumors. The 5-year overall survival rate for individuals diagnosed with GBM has been consistently less than 10% for over 50 years [1,2]. Immune checkpoint therapy (ICT) has dramatically altered the clinical outcomes of several cancer patients, revolutionizing the field of cancer treatment and establishing ICT alongside traditional treatment modalities as a pillar of cancer care [3]. One of the most important immunotherapies is the inhibition of the programmed death-1/programmed death-ligand 1 (PD-1/PD-L1) signaling pathway, which is frequently used by cancers to evade immune elimination. However, for GBM, anti-PD-1/PD-L1 monotherapy has yielded few satisfactory results in clinical studies [4].

Various preclinical experiments have highlighted the potential benefits of combining anti-PD-1/PD-L1 treatment with radiotherapy (RT) in boosting the effectiveness of therapeutic interventions [5,6]. Following irradiation, PD-L1 expression is upregulated in tumor tissues. Without any intervention, this promotes RT resistance [7]. However, by subsequently targeting the PD-L1 pathway, the tumor's evasion strategy can be exploited by clinicians [8]. Although this combination has demonstrated synergistic outcomes, pinpointing the exact mechanisms and processes behind this enhanced interaction has been challenging, largely because of the variability observed in PD-L1 expression levels after irradiation [9]. Studies have shown that not all tumors

---

* Corresponding author.
** Corresponding author.
E-mail addresses: zgliu0704@sina.com (Z. Liu), mhu@sdfmu.edu.cn (M. Hu).

https://doi.org/10.1016/j.jpha.2024.101082

exhibit enhanced PD-L1 expression after RT, leading to varying windows of opportunity for immunotherapeutic intervention [10,11]. Monitoring the dynamics of PD-L1 in glioma RT is thus necessary to properly gauge the optimal period for combined anti-PD-L1 therapy. Furthermore, real-time monitoring of PD-L1 expression has important clinical implications for identifying optimal RT doses and dose-fractionation schedules. In brief, the identification of patients with early PD-L1 upregulation following RT is vital in determining the population that would most likely benefit from combination immunotherapy.

Currently, the evaluation of tumor PD-L1 levels primarily relies on biopsy and immunohistochemical (IHC) analysis [12]. However, the fluctuating nature of immune checkpoint target expression has been recognized, revealing the limitations of single timepoint biopsies for capturing a complete expression profile during treatment. Therefore, molecular imaging is prominently used to provide ongoing, in-depth observations of target expression, serving to augment the data obtained from traditional IHC methods [13]. PD-L1 positron emission tomography/computed tomography (PET/CT) imaging has been proven valuable in cancer through clinical research. Anti-PD-L1 antibodies were initially developed as radiotracers due to their high binding affinity and specificity for PD-L1 [14,15]. For instance, ^{89}Zr-atezolizumab signal in tumors, measured several days after the injection of radiotracers, more accurately predicted the response to atezolizumab therapy than IHC or RNA analysis [16]. However, the prolonged serum half-life and slow clearance of radiolabeled monoclonal antibody (mAb) probes have some drawbacks—the necessity of extended time to achieve optimal tumor-to-background ratios (3–7 days) and the incidental radioactivity of the probes themselves, which impart relatively high radiation doses to patients. These limitations constrain the clinical use of radiolabeled mAb probes [13]. Moreover, mAbs are not ideal for brain tumor imaging because of their large molecular size, which hinders tissue penetration.

Although nanobodies demonstrate strong tumor penetration and rapid clearance *in vivo*, their production is labor-intensive, and their scaffolds require sophisticated genomics or proteomics technologies [17–20]. In contrast, small PD-L1-binding agents with low molecular weight, such as protein scaffolds and peptides, have been reported to bind PD-L1 with high affinity and have garnered significant attention for the development of novel PD-L1-targeting probes. Peptides, in particular, show significant potential for overcoming the limitations of mAb and nanobody-based probes [21–23]. Peptides are easy to synthesize, possess good thermal stability for isotope labeling, have low molecular weight, and exhibit rapid clearance and high tumor permeability. Therefore, peptide radiolabeling is emerging as a promising candidate for brain tumor immunoimaging [24]. Cyclic peptide 6297 (CP2), which originates from a Bristol–Myers Squibb (New York, NY, USA)-patented macrocyclic inhibitor of PD-1/PD-L1 and CD80 (B7-1)/PD-L1 interactions, demonstrates nanomolar affinity toward PD-L1 [25]. This cyclic peptide has two additional hydrophilic carboxyl groups compared with WL12 (a cyclic peptide), which significantly reduces nonspecific accumulation in the liver.

In this study, we synthesized a radiolabeled tracer derived from polyethylene glycol-modified CP2, which enables high-resolution and specific imaging of tumor PD-L1. Subsequently, we examined the capacity of this radiotracer to noninvasively determine PD-L1 expression levels in orthotopic xenograft GBM models and track alterations in PD-L1 expression caused by radiation therapy. Furthermore, we tested various RT doses and fractions in these models.

2. Materials and methods

2.1. Chemicals and equipment

Chemicals used in this study were procured from Sigma-Aldrich (St. Louis, MO, USA), unless otherwise specified. NOTA-PEG3-CP2 (NOTA-PCP2) was custom synthesized by GL Biochem Co., Ltd. (Shanghai, China). Aqueous [^{18}F]Fluoride was generated via an ^{18}O (p,n) ^{18}F nuclear reaction performed using a mini-trace cyclotron (9.6 MeV, GE Healthcare, Waukesha, WI, USA) with a 2.0 mL silver target. For irradiation, the enriched [^{18}O] water (97%) was procured from Cambridge Isotope Laboratories (Tewksbury MA, USA). PET/CT imaging was performed using a small-animal PET/CT scanner (IRIS PET/CT, Inviscan, Strasbourg, France). Radio-high-performance liquid chromatography (radio-HPLC) analysis was performed on a Shimadzu Nexera HPLC system (Shimadzu, Kyoto, Japan) with an XBridge C_{18} (4.6 mm × 150 mm, 3.5 μm) chromatographic column purchased from Waters Corporation (Milford, MA, USA). All cell culture and biological experiment-related reagents were purchased from Gibco (Thermo Fisher Scientific, Waltham, MA, USA).

2.2. Synthesis of [^{18}F]AlF-NOTA-PCP2

NOTA-PEG3-CP2 (NOTA-PCP2), which has a purity of >95% and was custom synthesized by GL Biochem (Shanghai, China), was used as a precursor for our study. We used 97%-pure $^{18}O{-}H_2O$ from Cambridge Isotope Laboratories (Tewksbury, MA, USA) for [^{18}F]F-production. Using the automated ChelationLab@Al^{18}F module, we synthesized [^{18}F]AlF-NOTA-PCP2. The process involved dissolving NOTA-PCP2 (80 nmol) in 20 μL of deionized water, adding 7 μL of 10 mM $AlCl_3$, 30 μL of 0.5M NaOAc-HOAc buffer (pH 4.2), 20 μL of 0.5 M ascorbic acid solution, and 300 μL of dimethylformamide (DMF) in a 2mL lyophilized tube. This mixture was sealed and heated at 100 °C for approximately 10 min, followed by C_{18} cartridge-based solid-phase extraction purification, to obtain the final pure tracer. For a comprehensive description of the methodology, refer to the detailed protocol provided in our previous publication [26].

2.3. Binding affinity assays

The binding affinities of PD-L1 and cyclic peptides were assessed using surface plasmon resonance (SPR) on a Biacore X100 system (Cytiva, Uppsala, Sweden). Recombinant PD-L1 protein was immobilized on a carboxymethylated dextran chip, with ethanol hydrochloride reducing nonspecific binding. PCP2, in concentrations ranging from 1.5625 to 100 nM, was flowed over the chip at a rate of 10 μL/min. The assay included 120 s for association, 300 s for dissociation, and chip regeneration with a 15 s glycine injection. The Biacore X100 system was used to analyze binding curves to calculate the dissociation constant (K_D).

2.4. Cell preparation and culture

GBM cell lines (i.e., U87MG, U251MG, U118MG, and A172), acquired from Haixing Biotechnology Co., Ltd. (Suzhou, China), were cultured in Dulbecco's modified Eagle medium supplemented with 10% fetal bovine serum (FBS) and 1% penicillin/streptomycin, undergoing regular mycoplasma tests. The cells were maintained at 37 °C in a 5% carbon dioxide atmosphere. To generate PD-L1 overexpressing (U87MG$^{PD-L1OE}$) or knockdown (U87MG$^{PD-L1KO}$) U87MG cells, lentiviral particles were purchased from Haixing

Biotechnology Co., Ltd.. U87MG cells were infected with the lentiviral particles and selected with puromycin. PD-L1 expression levels were verified by flow cytometry. Cells received 8 Gy irradiation using an RS2000-225 biological irradiator (Rad Source Technologies, Inc., Suwanee, GA, USA).

2.5. Cell-binding assays

In the *in vitro* cell-binding experiment, 1 × 10^6 cells were incubated with ~0.1 μCi of [^{18}F]AlF-NOTA-PCP2 for 1 h at 4 °C. After incubation, the cells were rinsed three times using cold phosphate-buffered saline (PBS) containing 0.1% Tween 20. The quantification of the cells was then performed using a Wizard 2 automated gamma counter (PerkinElmer, Waltham, MA, USA). The proportion of the administered dose (percentage of injected dose (% ID)) was determined by accounting for radioactive decay and normalizing to external [^{18}F]AlF-NOTA-PCP2 standards, which were examined in quadruplicate. To ensure precision and reliability, cellular uptake of radioactivity was measured four times for all cell lines, and this process was repeated three times.

2.6. Flow cytometry

Flow cytometry was utilized to determine PD-L1 expression on the surfaces of cells. This was done by employing a phycoerythrin-conjugated anti-PD-L1 antibody (clone 29 E.2A3, BioLegend, San Diego, CA, USA). The cells were treated with the antibody in fluorescence-activated cell sorting buffer (PBS, 1% FBS, 2 mM ethylenediaminetetraacetic acid) for 60 min at 4 °C. After that, they were washed and examined using an LSRFortessa flow cytometer (BD Biosciences, San Jose, CA, USA) to assess mean fluorescence intensity.

2.7. Xenograft models and treatment

Female nonobese diabetic/severe combined immunodeficiency (NOD/SCID) mice (4–5 weeks old) were purchased from Beijing Huafukang Biotechnology Co., Ltd. (Beijing, China). Animal studies were approved by the Animal Care and Use Committee of Shandong Cancer Hospital and Institute (Approval number: 2023001012). NOD/SCID mice received subcutaneous injections of 5 × 10^6 cells in 100 μL saline for subcutaneous tumor models. For intracranial glioma xenografts, 1.5 × 10^5 GBM cells were injected into the left striatum, guided by coordinates detailed previously [18]. Tumor development after implantation was monitored with weekly T2-weighted magnetic resonance imaging (MRI) scans. Brain tumors confirmed by MRI were identified in mice using PET/CT imaging; mice exhibiting severe neurological symptoms were euthanized. For mice inoculated with three tumors, the cumulative volume was carefully monitored to ensure that it did not exceed 1500 mm^3. Animals were humanely euthanized if they exhibited severe distress or when tumor volumes approached the maximum threshold, according to American Veterinary Medical Association-approved methods.

2.8. In vivo PET/CT imaging and ex vivo biodistribution in mouse xenograft models

The imaging procedure involved injecting saline radiotracers (100 μL, 5.55 ± 0.93 MBq) into the veins of anesthetized mice. One hour later, a microPET/CT imaging system (Inviscan SAS, Strasbourg, France) was used to conduct static PET/CT scans. Sequential dynamic scans occurred at 15–120-min intervals. Cold probe blocking involved a simultaneous injection of a 50 μg affibody; for antibody inhibition, mice received atezolizumab (20 mg/kg) one day before the scan. We measured the percentage of injected dose per cubic centimeter (% ID/cc) by reconstructing scans on OsiriX MD 11 using three-dimensional ordered subset expectation maximization/statistical parametric mapping with an emphasis on tumor regions of interest. Following euthanasia, the organs, tumors, blood, and percentage of injection dose per gram (% ID/g) were measured by γ-counting, after which decay correction was applied.

2.9. IHC and multicolor immunofluorescence

Before being sectioned for microscopy, brain and tumor samples were formalin-fixed and embedded in paraffin. Sections were then incubated with an anti-PD-L1 antibody (#13684, Cell Signaling Technology, Danvers, MA, USA) at a 1:400 dilution overnight at 4 °C. After incubation, sections were treated with horseradish peroxidase (SM802, Agilent, Santa Clara, CA, USA) and diaminobenzidine (Dako, Glostrup, Denmark) plus chromogen for 20 and 10 min, respectively. A ZEISS automatic digital slide scanner (Axio Scan. Z1, Oberkochen, Germany) was used to digitize the images, and ZEN 2012 software was used for analysis.

2.10. Blood and organ toxicity testing

As part of toxicological investigations, control mice received an intravenous injection of 100 μL saline, whereas treated mice received a 5 MBq dose of [^{18}F]AlF-NOTA-PCP2. Laboratory tests were performed 12, 24, and 72 h following imaging to measure alanine aminotransferase (ALT), aspartate aminotransferase (AST), blood urea nitrogen (BUN), creatinine (Cr), creatine kinase (CK), and creatine kinase-MB (CK-MB). For histopathological examination, samples of the heart, liver, spleen, lungs, and kidneys were stained with hematoxylin and eosin (H&E) and analyzed using the ZEISS slide scanner mentioned above.

2.11. MRI

MRI examinations were performed using a 9.4 T (T) Bruker BioSpec 94/30 scanner (Bruker, Ettlingen, Germany), as previously described [27]. This scanner features a gradient strength of up to 660 mT/m and a slew rate of 4570 T/m/s. Tumor localization was achieved using initial coronal and axial scout images. For T1-weighted scans, gadoteric acid glucosamine (1 μmol/g) was intravenously injected 5 min prior. The scan parameters were as follows: echo time (TE) of 6 ms, repetition time (TR) of 800 ms, excitation angle of 90°, field of view (FOV) of 4.0 × 3.0 cm^2, matrix size of 256 × 256, slice thickness of 0.8 mm, and 18 repetitions for each slice.

2.12. Radiation therapy and CT imaging

The Small Animal Radiation Research Platform (Xstrahl, Surrey, UK) was used for the precise targeting of orthotopic tumors with radiation, achieving human-like radiation therapy precision as previously described [28]. MRI scans guided tumor targeting before radiation, which was delivered using a 3 mm collimator at 220 kV and 13.0 mA, administering a total dose of 10–15 Gy to mice. Detailed radiation planning and dose distribution are illustrated in Figs. S1–S3.

2.13. Statistical analysis

The data in this study are presented as means ± standard deviations. We used one- or two-way analysis of variance and unpaired Student's *t*-tests to determine statistical significance of the datasets. *P*-values <0.05 were considered statistically significant for all analyses. Statistical analyses were performed using Prism 8 (GraphPad Prism, version 8.0.2).

3. Results

3.1. Radiochemical properties and synthesis of [^{18}F]AlF-NOTA-PCP2

PCP2, which is a polyethylene glycol-modified derivative of cyclic peptide 6297 designed to target PD-L1, comprises a 14-amino acid chain that includes three carboxylate groups and a free lysine amine. Compared with WL12, its hydrophilicity is notably enhanced by two additional carboxylic acid moieties (Fig. 1A). For Al^{18}F radiofluorination, PCP2 was further modified by incorporating 1,4,7-triazacyclononane-1,4,7-triacetic acid (NOTA) as a chelator. Synthesized efficiently in 25 min using ChelationLab@Al^{18}F (Fig. S4), [^{18}F]AlF-NOTA-PCP2 achieved 41% ± 4% (n = 20) non-decay-corrected yields and >95% purity (Fig. 1B). Its molar activity ranged between 37 and 55 GBq/μmol. Under a macroscopic inspection, the tracer was transparent and colorless, with a pH between 6.5 and 7. Table S1 presents the quality parameters. *In vitro* stability in 0.9% sodium chloride and 5% human serum albumin was confirmed, maintaining a radiochemical purity of >95% for up to 4 h (Fig. 1C).

3.2. [^{18}F]AlF-NOTA-PCP2 in vitro evaluation

Fig. 2A shows the binding interactions of PCP2 with recombinant human and murine PD-L1 protein as evaluated by SPR. K_D of PCP2 binding to human PD-L1 protein was determined to be 0.24 nM, in stark contrast to a K_D of 3.769×10^4 nM for its interaction with murine PD-L1 recombinant protein (Fig. S5). These results emphasize the species-specific binding affinity of PCP2, showing a marked preference and high selectivity for human PD-L1 over murine PD-L1.

For the purpose of assessing the specificity of [^{18}F]AlF-NOTA-PCP2 for PD-L1, we conducted cell-binding assays. These assays involved a range of glioma cell lines with varying levels of PD-L1 expression, including some that were genetically modified to either reduce or increase PD-L1 expression. The measurement of [^{18}F]AlF-NOTA-PCP2 radioactivity demonstrated a distinct pattern: U251MG > U118MG > A172 in natural cell lines and U87MG$^{PD-L1OE}$ > U87MG > U87MG$^{PD-L1KO}$ in genetically modified cell lines. This uptake pattern mirrored PD-L1 expression levels, as confirmed by flow cytometry. Cells with lower PD-L1 levels, particularly A172 and U87MG$^{PD-L1KO}$, showed reduced [^{18}F]AlF-NOTA-PCP2 binding. In addition, when conducting binding assays with a 1 μM excess of the nonradioactive PCP2 peptide, it was observed that there was a significant 90% decrease in radioactivity uptake by PD-L1-positive cells. This finding confirms the specificity of the assay ($P < 0.001$). (Figs. 2B–E).

An evaluation was also conducted to assess the capability of [^{18}F]AlF-NOTA-PCP2 in detecting changes in PD-L1 expression following interferon-gamma (IFNγ) treatment at a concentration of 200 IU/mL for 24 h. Cell-binding assays showed a notable increase in [^{18}F]AlF-NOTA-PCP2 uptake in U118MG cells following IFNγ treatment, compared to the PBS control (0.518% ± 0.066% vs. 0.22% ± 0.017% ID; $P < 0.001$) (Fig. 2F). This finding was further confirmed by flow cytometry (Fig. 2G). Furthermore, [^{18}F]AlF-NOTA-PCP2 exhibited a noteworthy capability to detect increased uptake in U87MG cells after irradiation, with a 28.11% enhancement in radiotracer uptake after treatment (0.49% ± 0.027% vs. 0.38% ± 0.049%; $P = 0.016$) (Fig. 2H), correlating with elevated PD-L1 expression on U87MG cells, as confirmed by flow cytometry (Fig. 2I). Collectively, these results establish a strong correlation ($R^2 = 0.87$; $P < 0.001$) between the uptake of [^{18}F]AlF-NOTA-PCP2 and the expression of PD-L1 (Fig. 2J). This provides compelling evidence that [^{18}F]AlF-NOTA-PCP2 specifically targets PD-L1 and inhibits the interaction between PD-1 and PD-L1.

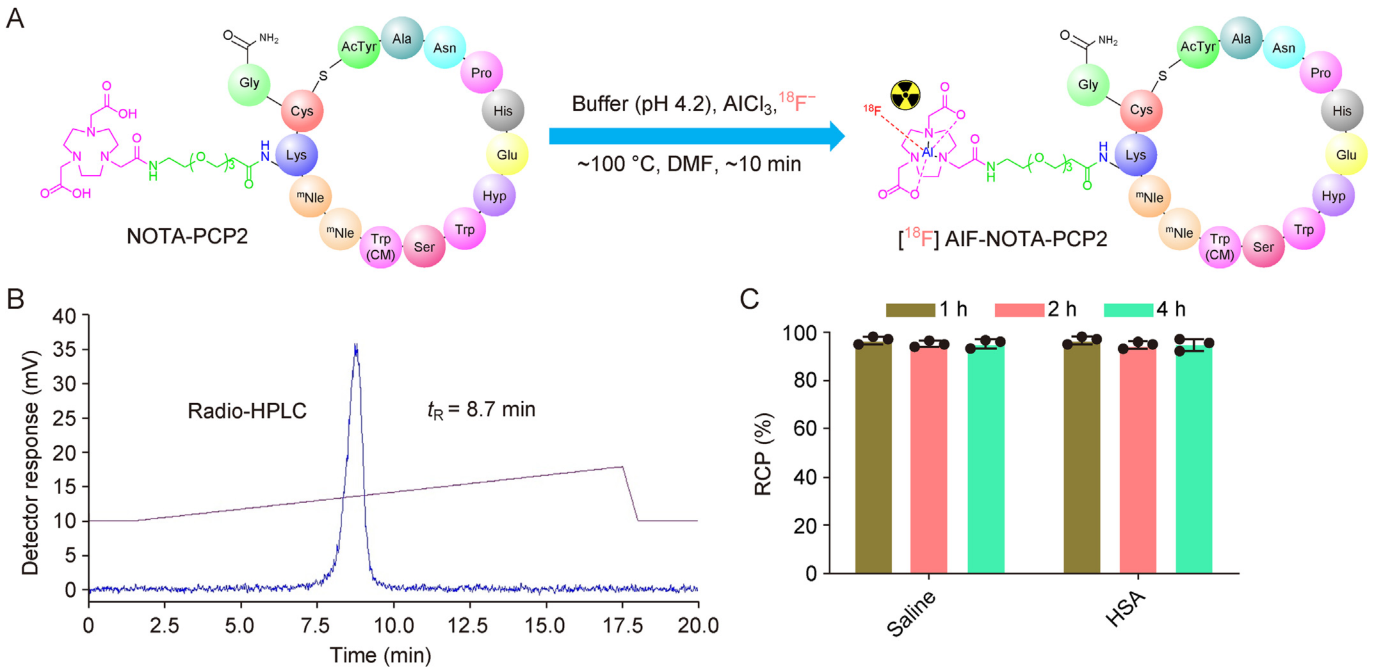

Fig. 1. Synthesis and characterization of [^{18}F]AlF-NOTA-PCP2. (A) Molecular structure and synthetic pathway of [^{18}F]AlF-NOTA-PCP2. (B) Verification of [^{18}F]AlF-NOTA-PCP2 synthesis, with radiochemical purity consistently above 95%. (C) High-performance liquid chromatography (HPLC) analysis showing >95% radiochemical purity (RCP) within a maximum of 4 h following synthesis. HSA: human serum albumin.

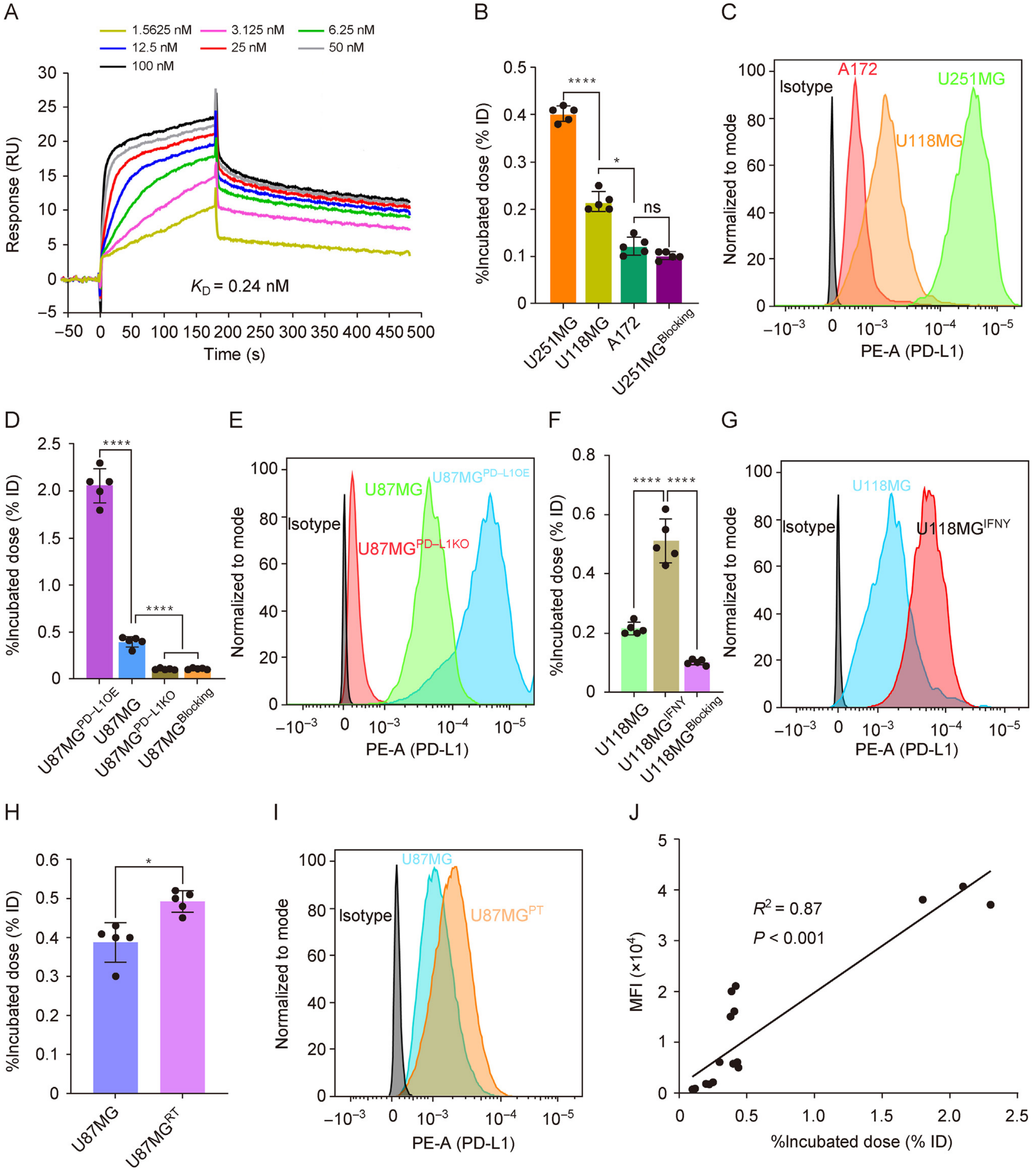

Fig. 2. *In vitro* specificity of [^{18}F]AlF-NOTA-PCP2 for programmed death-ligand 1 (PD-L1). (A) Surface plasmon resonance (SPR) analysis confirmation of PCP2's high-affinity binding to human PD-L1, characterized by a low equilibrium dissociation constant ($K_D \approx 0.24$ nM). (B) Cell-binding assays in wild-type glioma cell lines indicated a [^{18}F]AlF-NOTA-PCP2 uptake sequence of U251MG > U118MG > A172, with excess PCP2 pretreatment significantly reducing uptake in U251MG cells. (C) Quantification of PD-L1 in various wild-type glioma cell lines by flow cytometry using phycoerythrin-conjugated antibodies confirmed the findings of the cell-binding assay. (D) In genetically engineered cell lines, [^{18}F]AlF-NOTA-PCP2 uptake ranked U87MG$^{\text{PD-L1OE}}$ > U87MG > U87MG$^{\text{PD-L1KO}}$, with excess PCP2 significantly reducing uptake in U87MG$^{\text{PD-L1OE}}$. (E) Flow cytometry results showed that the expression of PD-L1 on the cell surface followed the order: U87MG$^{\text{PD-L1OE}}$ > U87MG > U87MG$^{\text{PD-L1KO}}$, which validated the cell-binding assay results. (F) Radiotracer uptake markedly increased in interferon-gamma (IFNγ)-treated (200 IU/mL, 24 h) U118MG cells and significantly decreased after PCP2 blockade. (G) Flow cytometry validated PD-L1 elevation after IFNγ treatment. (H, I) Cell-binding assays revealed enhanced [^{18}F]AlF-NOTA-PCP2 uptake in U87MG cells following 8 Gy irradiation ($P = 0.016$) (H), with flow cytometry confirming increased PD-L1 after radiotherapy (I). (J) Correlation analysis illustrating a strong relationship ($R^2 = 0.87$, $P < 0.001$) between mean fluorescence intensity (MFI) and [^{18}F]AlF-NOTA-PCP2 uptake. Error bars represent standard deviation ($n = 5$), significance assessed using the unpaired Student's *t*-test (ns: $P > 0.05$, $^{*}P < 0.05$, $^{****}P < 0.001$). U251MG$^{\text{Blocking}}$: cold probe blocking experiment in U251MG glioma cells; U87MG$^{\text{RT}}$: U87MG glioma cells receiving radiation therapy (RT).

3.3. Investigation of the toxicological characteristics of [^{18}F]AlF-NOTA-PCP2 in animal models

To assess the toxicity of [^{18}F]AlF-NOTA-PCP2, extensive analyses were performed, including complete blood counts, serum biochemistry, histopathological examinations, and observation of physical and behavioral changes. Critical markers for cardiac, renal, and hepatic functions, such as CK, CK-MB, BUN, Cr, ALT, and AST, were monitored. These indicators, along with body weight and general appearance, showed no significant differences between the [^{18}F]AlF-NOTA-PCP2 and control groups, even at varied intervals after injection (i.e., 12, 24, and 48 h) (Fig. S6). Furthermore, routine blood tests and pathological examinations, including H&E staining of vital organs, revealed no notable morphological changes or signs of organ damage, inflammation, or necrosis (Fig. S7). These results collectively suggest that [^{18}F]AlF-NOTA-PCP2 is not associated with acute or subchronic organ dysfunction or tissue toxicity.

3.4. An assessment of the pharmacokinetics and biodistribution of [^{18}F]AlF-NOTA-PCP2 in living organisms

To elucidate the pharmacokinetics and biodistribution of [^{18}F]AlF-NOTA-PCP2, PET imaging studies were conducted on NOD/SCID mice with U87MG xenografts. The PET images taken at 10, 30, 60, 90, and 120 min after injection revealed significant radiotracer accumulation in tumors as early as 10 min (Fig. 3A). Note that the kidney and bladder tissue samples exhibited the highest accumulation, aligning with the tracer's increased hydrophilicity and subsequently enhanced renal clearance. A pronounced tumor contrast was noted between 60 and 120 min, which was attributable to the clearance of background radiotracers. Before imaging, the administration of 2 mg/kg nonradioactive PCP2 markedly diminished tracer uptake in U87MG xenografts, underscoring the specificity of [^{18}F]AlF-NOTA-PCP2 for PD-L1. Furthermore, tumor-bearing mice received a single intravenous dose of atezolizumab (20 mg/kg) or saline 24 h before [^{18}F]AlF-NOTA-PCP2 PET/CT imaging. In atezolizumab-treated tumors, a substantial decrease in radioactivity accumulation was observed, suggesting fewer available PD-L1 interaction sites than that in saline-treated controls (Fig. 3B). These findings imply an overlap in the interaction surfaces of PD-L1:PCP2 and PD-L1:PD-1 antibodies, thereby validating the use of [^{18}F]AlF-NOTA-PCP2 for both qualitative and quantitative assessments of PD-L1 targeting in tumors *in vivo* by atezolizumab.

At 10, 30, 60, 120, and 180 min following radiotracer injection, we conducted a battery of *ex vivo* measures to validate imaging study results and evaluate the biodistribution of [^{18}F]AlF-NOTA-PCP2 in healthy tissue (Table S2). The biodistribution results showed a clear and long-lasting buildup of [^{18}F]AlF-NOTA-PCP2 in U87MG tumors, as indicated by the time-activity curves (Fig. 3C). This was paralleled by a consistent reduction in radioactivity levels over time in the blood, muscle, and other tissues, enhancing the contrast of the imaging (Fig. 3D). Echoing the PET/CT scan results, a higher uptake of [^{18}F]AlF-NOTA-PCP2 was detected in

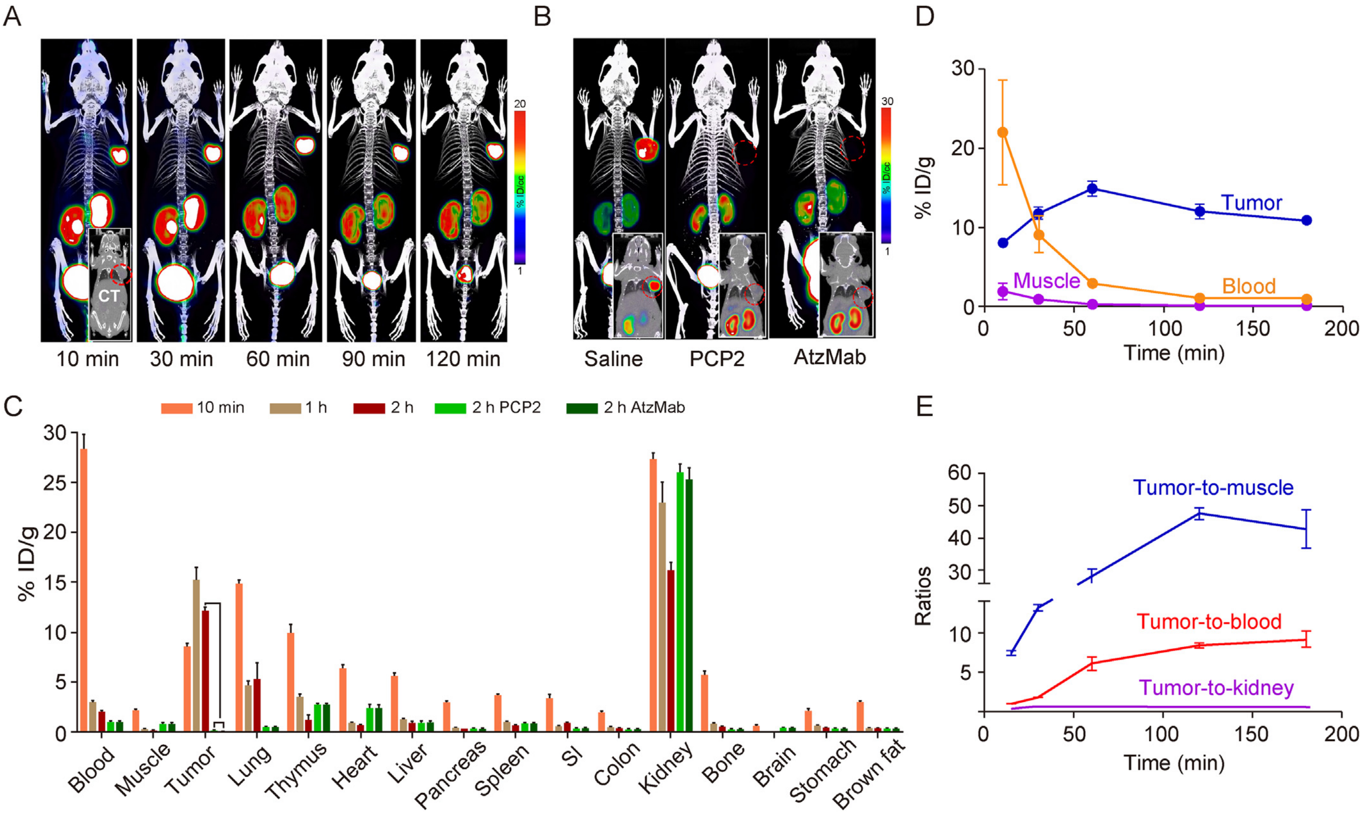

Fig. 3. Pharmacokinetics and biodistribution of [^{18}F]AlF-NOTA-PCP2 in U87MG tumors. (A) Micro-positron emission tomography/computed tomography (MicroPET/CT) imaging captured 10–120 min after injection of [^{18}F]AlF-NOTA-PCP2 in U87MG tumor-bearing mice, demonstrating a pronounced tumor-to-background ratio peak at 60 min. (B) Notable reduction in radioactivity uptake observed in U87MG tumors after blockade with 50 mg unlabeled PCP2, affirming [^{18}F]AlF-NOTA-PCP2's PD-L1 specificity. Tumor-bearing mice, injected with atezolizumab (AtzMab; 20 mg/kg) or saline 24 h before imaging, demonstrated reduced radioactivity in the AtzMab group, highlighting the effectiveness of [^{18}F]AlF-NOTA-PCP2's for PD-L1 targeting assessment *in vivo*. (C) Detailed biodistribution analysis of [^{18}F]AlF-NOTA-PCP2 in nonobese diabetic/severe combined immunodeficiency (NOD/SCID) mice with U87MG xenografts at 10 min, 1 h, and 2 h after injection. (D) [^{18}F]AlF-NOTA-PCP2 pharmacokinetics detailed in tumor, blood, and muscle tissues. (E) Time-activity curves, derived from biodistribution data. Error bars indicate standard deviation (SD) ($n = 3$). Significance was determined using the unpaired Student's *t*-test, $^{****}P < 0.001$.

the tumor and kidney tissue samples. The tumor-to-blood ratio at 60 min was 6.06 ± 0.68, while the tumor-to-muscle ratio at the same time point was 28.21 ± 1.89 (Fig. 3E). Applying a blocking dose of PCP2 in mice resulted in an 85.2% decrease in [^{18}F]AlF-NOTA-PCP2 uptake ($P < 0.001$) (Fig. 3C). Moreover, the administration of a single dose of atezolizumab (20 mg/kg) resulted in a substantial decrease of 92.2% in tracer uptake in U87MG tumors ($P < 0.001$) (Fig. 3C). The *in vitro* biodistribution measurements further corroborated the effectiveness of PET/CT imaging (Fig. 3B). Overall, the *in vivo* pharmacokinetics and *in vitro* biodistribution findings decisively validated [^{18}F]AlF-NOTA-PCP2's enhanced hydrophilicity and its specific targeting of PD-L1, reinforcing its efficacy in tumor imaging.

3.5. Estimates of human radiation dosimetry

Radiation dosimetry for human organs estimates for [^{18}F]AlF-NOTA-PCP2 was derived from its biodistribution data and analyzed using OLINDA/EXM 2.0. These estimates, corrected for decay, provided the absorbed dose values in various organs, based on F-18's pharmacokinetics using a female adult reference human phantom. Table S3 displays the comprehensive estimations of absorbed radiation doses in several human organs. The highest radiation dose from [^{18}F]AlF-NOTA-PCP2 was detected in the kidneys (9.91×10^{-3} mSv/MBq), followed by the lungs (7.2×10^{-3} mSv/MBq) and thymus (5.74×10^{-3} mSv/MBq). The overall effective dose of [^{18}F]AlF-NOTA-PCP2 was calculated to be 0.038 mSv/MBq, translating to an effective dose of 14.06 mSv for a human subject administered with 370 MBq (10 mCi) of [^{18}F]AlF-NOTA-PCP2.

3.6. [^{18}F]AlF-NOTA-PCP2 targeting of PD-L1 in the brain

We developed a clinically relevant orthotopic tumor model by stereotactically implanting GBM cells into the striatum of NOD/SCID mice brains, thereby facilitating the evaluation of the precision of [^{18}F]AlF-NOTA-PCP2 in detecting PD-L1^{+} cells in intracranial malignancies with notable specificity. PET/CT images acquired 1 h after radio-conjugate injection revealed a distinct and superior accumulation of [^{18}F]AlF-NOTA-PCP2 in U251MG tumors (9.51% ± 0.4%), previously delineated by T2-weighted MRI (Fig. 4A). We conducted supplementary gadolinium-diethylenetriamine penta-acetic acid (Gd-DTPA)-enhanced MRI to ascertain tumor margins and evaluate the integrity of the blood-brain barrier (BBB). The significant enhancement observed on MRI scans, which indicates BBB disruption, the regions of high uptake on PET/CT imaging employing [^{18}F]AlF-NOTA-PCP2 were directly correlated. This finding underscores that BBB disruption, as revealed by MRI enhancement, is crucial for cerebral imaging of [^{18}F]AlF-NOTA-PCP2. The examination of macroscopic specimens and brain slices stained with H&E confirmed the existence of clearly defined tumor

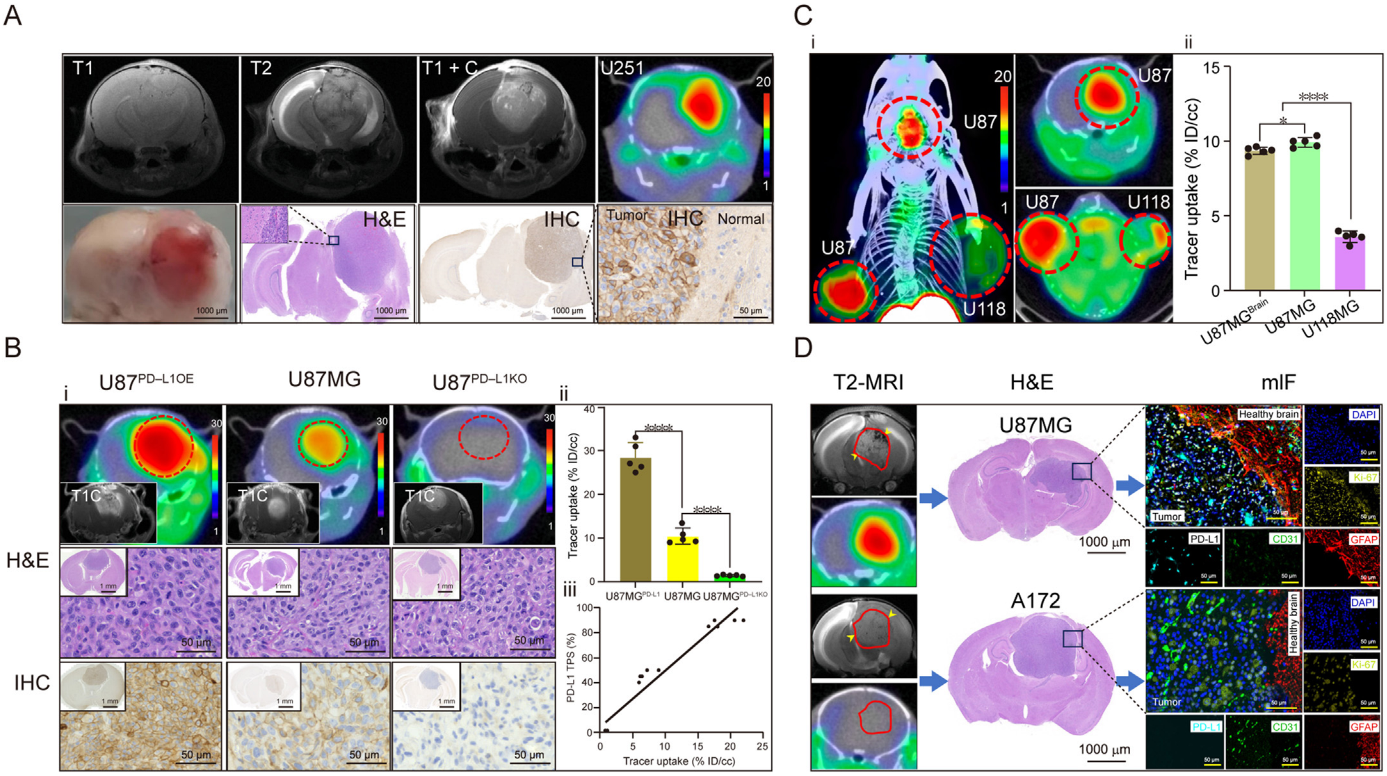

Fig. 4. [^{18}F]AlF-NOTA-PCP2 in precise programmed death-ligand 1 (PD-L1) detection in brain tumors. (A) U251MG orthotopic tumor model demonstrates [^{18}F]AlF-NOTA-PCP2's PD-L1 targeting in the brain. Magnetic resonance imaging (MRI) identified tumor location and blood-brain barrier (BBB) disruption, correlated with high [^{18}F]AlF-NOTA-PCP2 uptake in positron emission tomography/computed tomography (PET/CT). Gross specimen and hematoxylin and eosin (H&E)-stained section confirmation of tumor presence, aligned with imaging results; immunohistochemistry (IHC) analysis showing high PD-L1 expression in U251MG tumors. (B) PD-L1 expression levels and [^{18}F]AlF-NOTA-PCP2 uptake in the brain. (i) [^{18}F]AlF-NOTA-PCP2 uptake in U87MG orthotopic xenograft tumors with varying PD-L1 expression levels, as confirmed by H&E staining and IHC PD-L1 staining. (ii) Region of interest (ROI) analysis: [^{18}F]AlF-NOTA-PCP2 uptake 2.72 times higher in U87$^{PD-L1OE}$ than U87MG in the brain (28.45% ± 3.02% vs. 10.46% ± 1.65% ID/cc). (iii) Significant correlation between [^{18}F]AlF-NOTA-PCP2 uptake and PD-L1 tumor proportion score (TPS) ($R^2 = 0.89$). (C) Comparison between brain and extracranial tumors. (i) Similar [^{18}F]AlF-NOTA-PCP2 uptake in both brain orthotopic and subcutaneous tumors. (ii) 5.62% ± 2.9% lower uptake in U87MG brain tumors compared to U87MG subcutaneous ($^{*}P = 0.019$) , indicating slight BBB impact.U87MG^{brain}: Orthotopic glioma formed by U87MG cells. (D) Multicolor immunofluorescence (mIF) revealed high PD-L1 expression in U87MG cells and low CD31 expression compared with A172 cells, which exhibited the opposite pattern. This suggests that the uptake rate of [^{18}F]AlF-NOTA-PCP2 is independent of vessel density. Error bars represent standard deviation ($n = 5$), and significance is assessed using the unpaired Student's *t*-test in (B) and paired Student's *t*-test in (C) (ns: $P > 0.05$, $^{*}P < 0.05$, $^{****}P < 0.001$). T1: T1-weighted image; T2: T2-weighted image; T1 + C: T1-weighted image with contrast enhancement.

masses within the brain, which aligns with the intensified signals found on MRI and PET/CT scans. IHC analysis revealed a significantly higher expression of PD-L1 in U251MG tumor tissues than in adjacent normal brain regions (Fig. 4A). Images showing a high tumor-to-background contrast ratio (tumor/normal brain: 12.29 ± 1.12) were produced because the radio-conjugate was minimally taken up by the healthy brain parenchyma.

For the purpose of confirming the effectiveness of [^{18}F]AlF-NOTA-PCP2 in identifying different levels of PD-L1 expression in the brain, we conducted PET imaging on GBM. This was done using a tumor model derived from three different cell lines, each with varying levels of PD-L1 expression (Fig. 4Bi). The uptake of [^{18}F]AlF-NOTA-PCP2 in U87MG$^{\text{PD-L1OE}}$ tumors was 2.72 times higher than that in U87MG tumors (28.45% ± 3.02% vs. 10.46% ± 1.65% ID/cc), whereas tumors from the U87MG$^{\text{PD-L1KO}}$ cell line showed substantially lower tracer uptake (1.41% ± 0.15% ID/cc) (Fig. 4Bii). IHC staining for PD-L1 on these orthotopic xenografts corroborated the PET/CT data. Subsequent analysis revealed a significant correlation between [^{18}F]AlF-NOTA-PCP2 uptake and the PD-L1 tumor proportion score (TPS) across different GBM orthotopic xenograft models ($R^2 = 0.89$; $P < 0.0001$) (Fig. 4Biii).

To investigate whether there is a difference in the uptake of [^{18}F]AlF-NOTA-PCP2 in brain orthotopic versus extracranial tumors, a triple-tumor model in NOD/SCID mice was used, comprising

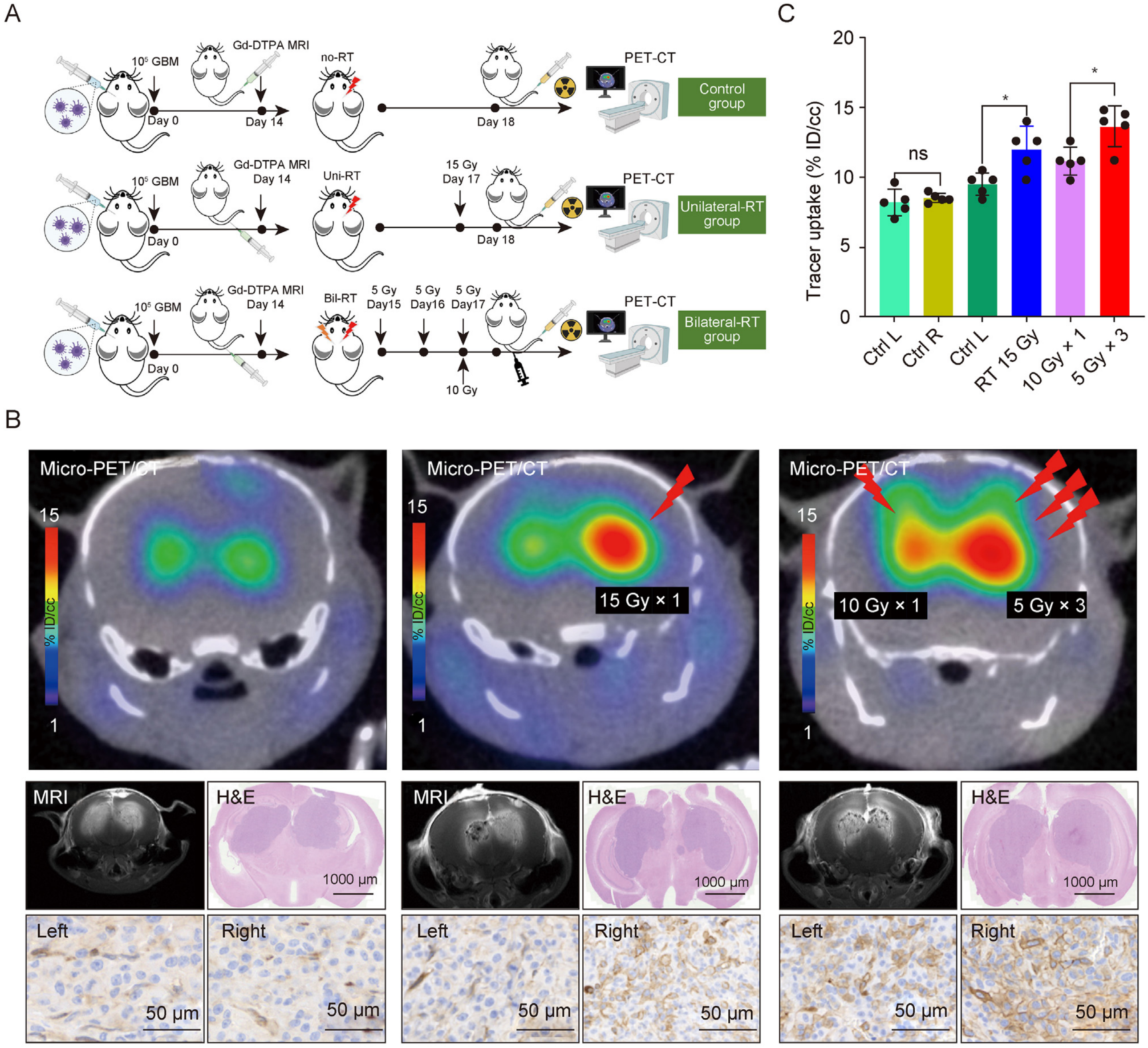

Fig. 5. [^{18}F]AlF-NOTA-PCP2 in imaging and quantifying radiation therapy (RT)-induced programmed death-ligand 1 (PD-L1) upregulation. (A) Workflow illustration of experimental and varied RT regimen groups. (B) [^{18}F]AlF-NOTA-PCP2 positron emission tomography/computed tomography (PET/CT) imaging of brain tumors under different RT regimens. This includes precise localization of intracranial doublet tumors via magnetic resonance imaging before PET/CT imaging, followed by post-imaging pathological analysis through hematoxylin and eosin (H&E) staining and PD-L1 immunohistochemistry. (C) Region of interest (ROI) analysis revealed enhanced [^{18}F]AlF-NOTA-PCP2 uptake after RT, with the unilateral 15 Gy group showing a significant increase (12.04% ± 1.43%) compared to the non-irradiated group (9.51% ± 0.73%; $P = 0.013$). Fractionated RT (5 Gy × 3) demonstrated greater PD-L1 upregulation effectiveness than a single dose (10 Gy × 1) (13.9% ± 1.54% ID/cc vs. 11.48% ± 1.05% ID/cc, $P = 0.029$). Error bars represent standard deviation ($n = 5$), and significance is assessed using the paired Student's t-test (ns: $P > 0.05$, $^*P < 0.05$). Ctrl R: right-side control; Ctrl L: left-side control.

U87MG brain orthotopic, U87MG subcutaneous, and U118MG subcutaneous tumors (Fig. 4Ci). We ensured more accurate radiotracer uptake measurements by focusing on tumors with diameters of at least 3 mm, which is three times the system resolution. PET/CT imaging showed a 5.62% ± 2.9% lower uptake in U87MG orthotopic tumors than in U87MG subcutaneous tumors ($P = 0.019$), suggesting minimal influence from the BBB (Fig. 4Cii). Note that in U87MG orthotopic tumors, [^{18}F]AlF-NOTA-PCP2 uptake was 2.6 ± 0.22 times higher than that in U118MG subcutaneous tumors (9.37% ± 0.21% vs. 3.61% ± 0.33% ID/cc), highlighting PD-L1 expression as a key determinant of uptake differences. Multicolor immunofluorescence (mIF) staining, including CD31 (Fig. 4D), revealed that the vascular density of U87MG orthotopic brain tumors was significantly lower than that of A172 tumors. However, [^{18}F]AlF-NOTA-PCP2 uptake in U87MG was significantly higher than that in A172 (10.46% ± 1.65% vs. 2.31% ± 0.83% ID/cc), reinforcing the predominance of PD-L1 expression over vascular density in influencing uptake. Consequently, this study demonstrates that microPET/CT imaging with [^{18}F]AlF-NOTA-PCP2 is highly effective in specifically and sensitively identifying aggressive brain tumors.

3.7. Noninvasive imaging and quantification of RT-induced PD-L1 upregulation with [^{18}F]AlF-NOTA-PCP2

To assess the ability of [^{18}F]AlF-NOTA-PCP2 to detect RT-induced upregulation of PD-L1 expression in brain tumors, we established an intracranial dual-tumor model. The experimental groups and RT protocols are presented in Fig. 5A. In the control group, the uptake rates of bilateral U87MG tumors were not significantly different (8.19% ± 0.86% vs. 8.51% ± 0.31% ID/cc, $P = 0.508$). In the unilateral radiation therapy group, the uptake rate on the side receiving 15 Gy irradiation was 12.04% ± 1.43%, which was significantly higher than that on the nonirradiated side (9.51% ± 0.73%; $P = 0.013$), providing evidence that radiation therapy can induce higher PD-L1 expression in orthotopic brain tumors. For the bilateral radiation therapy group, one tumor side was treated with a 5 Gy × 3 fraction radiation therapy regimen, whereas the other side received an equivalent dose of 10 Gy. The results showed that the uptake in the 5 Gy × 3 fraction group (13.9% ± 1.54% ID/cc) was significantly higher than that in the 10 Gy × 1 fraction group (11.48% ± 1.05% ID/cc, $P = 0.029$), further indicating that a fractionated radiation therapy regimen is more effective in inducing PD-L1 upregulation (Figs. 5B and C). Furthermore, mIF staining revealed PD-L1 expression in these tissues; however, no increase in vascular density (CD31) was observed following RT (Fig. S8).

4. Discussion

Immunotherapy, particularly PD-1/PD-L1 inhibitors, has revolutionized cancer treatment; however, its efficacy in GBM has been limited. Studies have shown that combining immunotherapy with RT can enhance treatment outcomes in many cancers [5,6,29,30]. However, clinical trials, such as CheckMate 143 and CheckMate 548, have not demonstrated significant survival benefits for patients with GBM using PD-1/PD-L1 inhibitors alone or in combination with RT and temozolomide [4,31]. Despite these mixed results, some long-term survivors in these trials had high baseline PD-L1 levels, suggesting a potential benefit in certain subgroups.

Tumor PD-L1 overexpression is a predictor of better outcomes with PD-1/PD-L1 inhibitors [32,33]. PD-L1 is often upregulated following irradiation [7]; however, not all tumors exhibit this increase [11]. Identifying patients with high baseline or early post-RT PD-L1 upregulation could enhance treatment efficacy. However, monitoring PD-L1 changes in brain tumors after RT remains challenging. Currently, IHC is the standard for assessing PD-L1 expression [34]. Nevertheless, PD-L1 is dynamic and evolves during cancer progression and treatment, making IHC insufficient for accurate monitoring [33].

Noninvasive nuclear imaging provides real-time, dynamic, and quantitative PD-L1 measurement in tumors [13]. Radionuclide probes, such as nuclide-labeled mAbs, nanobodies, and peptide molecules, have advanced preclinical and early-phase clinical research [35–38]. Small-molecule inhibitors like ^{68}Ga-BMS-986192 and nanobody-based antibodies like ^{68}Ga-NODA-CDV-Nb109, show high PD-L1 affinity and significant clinical potential [39–42]. However, few radiotracers focus on noninvasively selecting GBM patients with high PD-L1 expression before and after RT [43]. Antibody-based imaging often struggles with BBB traversal because of the large molecular size of macromolecules [44]. In contrast, small-molecule peptide probes, such as [^{18}F]AlF-NOTA-PCP2, offer enhanced tissue penetration and rapid clearance, making them particularly suitable for brain tumor imaging. Furthermore, the [^{18}F]AlF label has higher availability, better spatial resolution, and a suitable half-life, enabling efficient and cost-effective imaging with reduced radiation exposure and improved spatial resolution in PET imaging. [^{18}F]AlF-NOTA-PCP2 is derived from the polyethylene glycol-modified cyclic peptide 6297, which combines small size with high tissue penetration. We developed and comprehensively evaluated this ^{18}F-labeled PET imaging agent for its specificity, *in vivo* toxicity, pharmacokinetics, biodistribution, and human radiation dose estimation.

Our evaluations demonstrate that [^{18}F]AlF-NOTA-PCP2 has high specificity for PD-L1 both *in vitro* and *in vivo*. PCP2 was found by SPR to bind firmly to PD-L1, with a K_D lower than that previously reported for ^{64}Cu-NOTA-WL12 (0.24 nM vs. 3.012 nM). Atezolizumab blockade assays revealed overlapping interaction surfaces of PD-L1:PCP2 and PD-L1:PD-1 antibodies, thereby validating the use of [^{18}F]AlF-NOTA-PCP2 in both qualitative and quantitative assessments of PD-L1 targeting in tumors *in vivo* by atezolizumab. PET/CT and biodistribution studies have showed that the nonspecific accumulation of [^{18}F]AlF-NOTA-PCP2 in the liver was significantly lower than that previously reported for ^{64}Cu-WL12 (0.937% ± 0.124% vs. 24.2% ± 2.5% ID/g). Furthermore, PET/CT revealed that [^{18}F]AlF-NOTA-PCP2 provides favorable tumor-to-normal tissue contrast as early as 1–2 h after injection, compared to the 1–3 days typically required for antibody-based imaging probes. Additionally, [^{18}F]AlF-NOTA-PCP2 PET features a 60 min injection-to-imaging interval, fitting well within the standard clinical workflow, and allows for repeated imaging of the same subject, which is essential for monitoring treatment-induced changes in PD-L1 dynamics. We also observed a good correlation between the tumor uptake of [^{18}F]AlF-NOTA-PCP2 and PD-L1 expression.

We observed significant [^{18}F]AlF-NOTA-PCP2 uptake in U251MG orthotopic tumors by PET/CT imaging (9.51% ± 0.4%), with specificity for intracerebral PD-L1 further validated in three orthotopic tumor models with different PD-L1 expression levels. A strong correlation ($R^2 = 0.89$; $P < 0.0001$) was observed between [^{18}F]AlF-NOTA-PCP2 uptake and the PD-L1 TPS. Furthermore, we confirmed the effectiveness of [^{18}F]AlF-NOTA-PCP2 in detecting elevated PD-L1 levels in U87MG orthotopic tumors after RT (12.04% ± 1.43% after RT vs. 9.51% ± 0.73% before RT, $P = 0.013$). Additionally, our research indicates that fractionated radiation regimens more effectively induce PD-L1 upregulation than single doses (13.9% ± 1.54% vs. 11.48% ± 1.05% ID/cc), underscoring the potential of [^{18}F]AlF-NOTA-PCP2 in optimizing RT protocols for improved immunotherapy outcomes. Collectively, our findings show that [^{18}F]AlF-NOTA-PCP2 is a promising tool for noninvasive detection of PD-L1 expression.

A crucial consideration when imaging brain tumors is the impact of these tumors on the BBB. Tumors disrupt the BBB's integrity, leading to structural changes that affect molecular permeability and efflux [45,46]. Dynamic contrast-enhanced MRI is widely used to noninvasively assess BBB damage [47]. Our study confirmed significant BBB disruption in GBM orthotopic tumors using Gd-DTPA-enhanced MRI, with the PET/CT imaging results correlating closely. Considering this, our objective was to confirm that the higher uptake of [^{18}F]AlF-NOTA-PCP2 was solely a result of increased PD-L1 expression within the tumor and not caused by increased vascular permeability. Fortunately, numerous facets of our results make this possible confounding factor unlikely. U87MG tumors exhibited higher [^{18}F]AlF-NOTA-PCP2 uptake but lower vascular density than A172 tumors, suggesting that vascular density is not the primary determinant of [^{18}F]AlF-NOTA-PCP2 uptake in brain tumors. Furthermore, within an orthotopic tumor of the same murine model, the uptake of [^{18}F]AlF-NOTA-PCP2 demonstrated a marginal decrease (5.56% ± 0.03%) compared to its uptake in the subcutaneous tumor. This finding suggests that despite the compromised integrity of the BBB, there was still a subtle but discernible effect on the incorporation of the radiotracer, indicating that the BBB was not completely without influence.

To minimize distortion caused by partial volume effects and enhance the accuracy of radiotracer uptake measurements, particularly in smaller brain tumors, we used a microPET/CT system with a spatial resolution of 1 mm, conforming to National Electrical Manufacturers Association standards. Our methodology focused on examining tumors at least three times larger (3 mm) than the system's resolution (1 mm). Overall, our microPET/CT studies in orthotopic GBM xenografts indicated that [^{18}F]AlF-NOTA-PCP2 effectively penetrates the disrupted BBB and targets PD-L1 in brain tumors, affirming its significant potential for accurat imaging of malignant gliomas.

Our work is naturally limited by the inherent differences between animal models and humans; a mouse is not a human, and thus, the dynamics of PD-L1 expression after RT in a mouse's brain cannot perfectly replicate those in a human brain. However, this only serves to underscore the need for safe, real-time, and noninvasive methods for evaluating dynamic PD-L1 expression in patients. Our investigation provided a proof-of-concept, demonstrating the potential of the novel small-molecule cyclic peptide tracer [^{18}F]AlF-NOTA-PCP2 in patient stratification for radioimmunotherapy. Further research is needed to determine the optimal dose and timing for radioimmunotherapy.

5. Conclusion

Our study pioneered the use of a highly permeable small-molecule cyclic peptide probe in PET/CT imaging to investigate dynamic PD-L1 changes after RT in orthotopic GBM models. The novel tracer [^{18}F]AlF-NOTA-PCP2, applied for the first time in brain tumor PET imaging, demonstrated high sensitivity and resolution in detecting tumor uptake. Monitoring changes in PD-L1 expression in brain tumors following different RT regimens could be facilitated with the use of [^{18}F]AlF-NOTA-PCP2 in PET imaging. Consequently, this probe has significant clinical and translational potential in paving the way for more personalized and effective cancer treatment strategies.

CRediT authorship contribution statement

Yong Wang: Writing – original draft, Software, Resources, Methodology, Investigation, Formal analysis, Data curation, Conceptualization. **Kewen He:** Writing – review & editing, Writing – original draft, Validation, Methodology, Investigation, Formal analysis. **Yang Zhang:** Formal analysis, Data curation. **Yunhao Chen:** Formal analysis, Data curation. **Shijie Wang:** Supervision, Resources. **Kunlong Zhao:** Resources. **Zhiguo Liu:** Writing – review & editing, Writing – original draft, Supervision, Resources, Conceptualization. **Man Hu:** Writing – review & editing, Writing – original draft, Supervision, Resources, Conceptualization.

Declaration of competing interest

The authors declare that there are no conflicts of interest.

Acknowledgments

This study received support from the National Natural Science Foundation of China (Grant Nos.: 82272751 and 82202958), the Natural Science Foundation of Shandong, China (Grant No.: ZR2021LSW002), and the Science and Technology Program of Jinan, China (Grant Nos.: 202225019 and 202225013) to Man Hu; the Shandong Postdoctoral Innovation Program, China (Grant No.: SDCX-ZG-202302011) and Beijing Science and Technology Innovation Medical Development Foundation, China (Grant No.: KC2023-JX-0288-BQ26) to Yong Wang ; the Natural Science Foundation of China (Grant No.: NSFC82303676), the Natural Science Foundation of Shandong (Grant No.: ZR2023QH208), the China Postdoctoral Science Foundation (Grant No.: 2023M732125), and the Taishan Scholar Project Special Fund (Grant No.: tsqn202312368) to Kewen He.

Appendix A. Supplementary data

Supplementary data to this article can be found online at https://doi.org/10.1016/j.jpha.2024.101082.

References

[1] L.R. Schaff, I.K. Mellinghoff, Glioblastoma and other primary brain malignancies in adults: A review, JAMA 329 (2023) 574–587.
[2] V. Venkataramani, Y. Yang, M.C. Schubert, et al., Glioblastoma hijacks neuronal mechanisms for brain invasion, Cell 185 (2022) 2899–2917.e31.
[3] A. Chow, K. Perica, C.A. Klebanoff, et al., Clinical implications of T cell exhaustion for cancer immunotherapy, Nat. Rev. Clin. Oncol. 19 (2022) 775–790.
[4] D.A. Reardon, A.A. Brandes, A. Omuro, et al., Effect of nivolumab vs bevacizumab in patients with recurrent glioblastoma: The CheckMate 143 phase 3 randomized clinical trial, JAMA Oncol. 6 (2020) 1003–1010.
[5] S.G.C. Kroeze, M. Pavic, K. Stellamans, et al., Metastases-directed stereotactic body radiotherapy in combination with targeted therapy or immunotherapy: Systematic review and consensus recommendations by the EORTC-ESTRO OligoCare consortium, Lancet Oncol. 24 (2023) e121–e132.
[6] L. Galluzzi, M.J. Aryankalayil, C. Norman Coleman, et al., Emerging evidence for adapting radiotherapy to immunotherapy, Nat. Rev. Clin. Oncol. 20 (2023) 543–557.
[7] X. Tu, B. Qin, Y. Zhang, et al., PD-L1 (B7-H1) competes with the RNA exosome to regulate the DNA damage response and can be targeted to sensitize to radiation or chemotherapy, Mol. Cell 74 (2019) 1215–1226.e4.
[8] Y. Wu, Y. Song, R. Wang, et al., Molecular mechanisms of tumor resistance to radiotherapy, Mol. Cancer 22 (2023), 96.
[9] G. Lei, C. Mao, Y. Yan, et al., Ferroptosis, radiotherapy, and combination therapeutic strategies, Protein Cell 12 (2021) 836–857.
[10] E.B. Ehlerding, H.J. Lee, T.E. Barnhart, et al., Noninvasive imaging and quantification of radiotherapy-induced PD-L1 upregulation with ^{89}Zr-df-atezolizumab, Bioconjug. Chem. 30 (2019) 1434–1441.
[11] M. Kikuchi, D.A. Clump, R.M. Srivastava, et al., Preclinical immunoPET/CT imaging using Zr-89-labeled anti-PD-L1 monoclonal antibody for assessing radiation-induced PD-L1 upregulation in head and neck cancer and melanoma, Oncoimmunology 6 (2017), e1329071.
[12] M. Yi, X. Zheng, M. Niu, et al., Combination strategies with PD-1/PD-L1 blockade: Current advances and future directions, Mol. Cancer 21 (2022), 28.
[13] S.P. Rowe, M.G. Pomper, Molecular imaging in oncology: Current impact and future directions, CA Cancer J Clin. 72 (2022) 333–352.
[14] D. Giesen, L.N. Broer, M.N. Lub-de Hooge, et al., Probody therapeutic design of ^{89}Zr-CX-072 promotes accumulation in PD-L1-expressing tumors compared to normal murine lymphoid tissue, Clin. Cancer Res. 26 (2020) 3999–4009.

[15] L. Kist de Ruijter, J.S. Hooiveld-Noeken, D. Giesen, et al., First-in-human study of the biodistribution and pharmacokinetics of 89Zr-CX-072, a novel immunopet tracer based on an anti-PD-L1 probody, Clin. Cancer Res. 27 (2021) 5325–5333.

[16] F. Bensch, E.L. van der Veen, M.N. Lub-de Hooge, et al., ^{89}Zr-atezolizumab imaging as a non-invasive approach to assess clinical response to PD-L1 blockade in cancer, Nat. Med. 24 (2018) 1852–1858.

[17] H. Hosseinkhani, Nanomaterials in Advanced Medicine, Wiley, Weinheim, 2019.

[18] H. Hosseinkhani, Biomedical Engineering: Materials, Technology, and Applications, John Wiley & Sons, Hoboken, 2022.

[19] Y. Xing, G. Chand, C. Liu, et al., Early phase I study of a ^{99m}Tc-labeled anti-programmed death ligand-1 (PD-L1) single-domain antibody in SPECT/CT assessment of PD-L1 expression in non-small cell lung cancer, J. Nucl. Med. 60 (2019) 1213–1220.

[20] G. Lv, X. Sun, L. Qiu, et al., PET imaging of tumor PD-L1 expression with a highly specific nonblocking single-domain antibody, J. Nucl. Med. 61 (2020) 117–122.

[21] A. Mishra, K. Gupta, D. Kumar, et al., Non-invasive PD-L1 quantification using [^{18}F] DK222-PET imaging in cancer immunotherapy, J. Immunother. Cancer 11 (2023), e007535.

[22] X. Zhou, J. Jiang, X. Yang, et al., First-in-humans evaluation of a PD-L1-binding peptide PET radiotracer in non-small cell lung cancer patients, J. Nucl. Med. 63 (2022) 536–542.

[23] C. Li, N. Zhang, J. Zhou, et al., Peptide blocking of PD-1/PD-L1 interaction for cancer immunotherapy, Cancer Immunol. Res. 6 (2018) 178–188.

[24] C.L. Charron, J.L. Hickey, T.K. Nsiama, et al., Molecular imaging probes derived from natural peptides, Nat. Prod. Rep. 33 (2016) 761–800.

[25] M.M. Miller, C. Mapelli, M.P. Allen, et al., Inventors; Macrocyclic inhibitors of the pd-1/pd-l1 and cd80(b7-1)/pd-l1 protein/protein interactions, B.-M. Squibb, patent WO2014151634A1, 25 September, 2014.

[26] Z. Liu, L. Yu, K. Cheng, et al., Optimization, automation and validation of the large-scale radiosynthesis of Al^{18}F tracers in a custom-made automatic platform for high yield, React. Chem. Eng. 5 (2020) 1441–1449.

[27] J. Zhang, X. Sun, H. Li, et al., *In vivo* characterization and analysis of glioblastoma at different stages using multiscale photoacoustic molecular imaging, Photoacoustics 30 (2023), 100462.

[28] X. Hu, M. Zhao, M. Bai, et al., PARP inhibitor plus radiotherapy reshape the immune suppressive microenvironment and potentiate the efficacy of immune checkpoint inhibitors in tumors with IDH1 mutation, Cancer Lett. 586 (2024), 216676.

[29] C.M. Jackson, J. Choi, M. Lim, Mechanisms of immunotherapy resistance: Lessons from glioblastoma, Nat. Immunol. 20 (2019) 1100–1109.

[30] P. Zhu, S. Li, J. Ding, et al., Combination immunotherapy of glioblastoma with dendritic cell cancer vaccines, anti-PD-1 and poly I: C, J. Pharm. Anal. 13 (2023) 616–624.

[31] M. Lim, M. Weller, A. Idbaih, et al., Phase III trial of chemoradiotherapy with temozolomide plus nivolumab or placebo for newly diagnosed glioblastoma with methylated MGMT promoter, Neuro Oncol. 24 (2022) 1935–1949.

[32] H. Yamaguchi, J.M. Hsu, W. Yang, et al., Mechanisms regulating PD-L1 expression in cancers and associated opportunities for novel small-molecule therapeutics, Nat. Rev. Clin. Oncol. 19 (2022) 287–305.

[33] H. Gao, Y. Wu, J. Shi, et al., Nuclear imaging-guided PD-L1 blockade therapy increases effectiveness of cancer immunotherapy, J. Immunother. Cancer 8 (2020), e001156.

[34] C. Luchini, F. Bibeau, M.L. Ligtenberg, et al., ESMO recommendations on microsatellite instability testing for immunotherapy in cancer, and its relationship with PD-1/PD-L1 expression and tumour mutational burden: A systematic review-based approach, Ann. Oncol. 30 (2019) 1232–1243.

[35] J. Llop, T. Lammers, Nanoparticles for cancer diagnosis, radionuclide therapy and theranostics, ACS Nano 15 (2021) 16974–16981.

[36] X. Sun, Y. Li, T. Liu, et al., Peptide-based imaging agents for cancer detection, Adv. Drug Deliv. Rev. 110-111 (2017) 38–51.

[37] M.P. Kelly, S. Makonnen, C. Hickey, et al., Preclinical PET imaging with the novel human antibody ^{89}Zr-DFO-REGN3504 sensitively detects PD-L1 expression in tumors and normal tissues, J. Immunother. Cancer 9 (2021), e002025.

[38] K. He, S. Zeng, L. Qian, Recent progress in the molecular imaging of therapeutic monoclonal antibodies, J. Pharm. Anal. 10 (2020) 397–413.

[39] D.J. Donnelly, J. Kim, T. Tran, et al., The discovery and evaluation of [^{18}F] BMS-986229, a novel macrocyclic peptide PET radioligand for the measurement of PD-L1 expression and *in-vivo* PD-L1 target engagement, Eur. J. Nucl. Med. Mol. Imaging 51 (2024) 978–990.

[40] S.L. Cytryn, N. Pandit-Taskar, M.A. Lumish, et al., ^{18}F-BMS-986229 PET to assess programmed-death ligand 1 status in gastroesophageal cancer, J. Nucl. Med. 65 (2024) 722–727.

[41] Y. Chen, S. Zhu, J. Fu, et al., Development of a radiolabeled site-specific single-domain antibody positron emission tomography probe for monitoring PD-L1 expression in cancer, J. Pharm. Anal. 12 (2022) 869–878.

[42] S. Robu, A. Richter, D. Gosmann, et al., Synthesis and preclinical evaluation of a ^{68}Ga-labeled adnectin, ^{68}Ga-BMS-986192, as a PET agent for imaging PD-L1 expression, J. Nucl. Med. 62 (2021) 1228–1234.

[43] G. Sharma, M.C. Braga, C. Da Pieve, et al., Immuno-PET imaging of tumour PD-L1 expression in glioblastoma, Cancers (Basel) 15 (2023), 3131.

[44] W.G. Lesniak, C. Chu, A. Jablonska, et al., A distinct advantage to intraarterial delivery of ^{89}Zr-bevacizumab in PET imaging of mice with and without osmotic opening of the blood-brain barrier, J. Nucl. Med. 60 (2019) 617–622.

[45] C.D. Arvanitis, G.B. Ferraro, R.K. Jain, The blood-brain barrier and blood-tumour barrier in brain tumours and metastases, Nat. Rev. Cancer 20 (2020) 26–41.

[46] H. Li, T. Ye, X. Liu, et al., The role of signaling crosstalk of microglia in hippocampus on progression of ageing and Alzheimer's disease, J. Pharm. Anal. 13 (2023) 788–805.

[47] C. Chu, A. Jablonska, Y. Gao, et al., Hyperosmolar blood-brain barrier opening using intra-arterial injection of hyperosmotic mannitol in mice under real-time MRI guidance, Nat. Protoc. 17 (2022) 76–94.